

10 Gbit s⁻¹ Free Space Data Transmission at 9 μm Wavelength With Unipolar Quantum Optoelectronics

Hamza Dely, Thomas Bonazzi, Olivier Spitz, Etienne Rodriguez, Djamel Gacemi, Yanko Todorov, Konstantinos Pantzas, Grégoire Beaudoin, Isabelle Sagnes, Lianhe Li, Alexander Giles Davies, Edmund H. Linfield, Frédéric Grillot, Angela Vasanelli, and Carlo Sirtori*

Free space optics data transmission with bitrate in excess of 10 Gbit s⁻¹ is demonstrated at 9 μm wavelength by using a unipolar quantum optoelectronic system at room temperature, composed of a quantum cascade laser, a modulator, and a quantum cascade detector. The large frequency bandwidth of the system is set by the detector and the modulator that are both high frequency devices, while the laser emits in continuous wave. The amplitude modulator relies on the Stark shift of an absorbing optical transition in and out of the laser frequency. This device is designed to avoid charge displacement, and therefore it is characterized by an intrinsically large bandwidth and very low electrical power consumption. This demonstration of high-bitrate data transmission sets unipolar quantum devices as the most performing platform for the development of optoelectronic systems operating at very high frequency in the mid-infrared for several applications, such as digital communications and high-resolution spectroscopy.

1. Introduction

Unipolar quantum optoelectronics (UQOs) comprises an ensemble of semiconductor devices operating at room temperature in the mid-infrared ($\lambda \approx 4\text{--}16\ \mu\text{m}$) with bandwidths of tens of GHz. The devices exploit the presence of quantum-confined 2D electronic states formed in the conduction band of technological mature semiconductors. They are thus unipolar as electrons are the only charge carriers present. UQOs enables the realization of optoelectronic systems that combine in phase different devices to produce complex functions and operations.^[1,2] In the mid-infrared this is highly sought after, not only for technological applications, but also to address fundamental physics questions. For example, highly

sensitive and ultrafast optoelectronic systems are required for free-space communications,^[3–6] light detection and ranging (LIDAR),^[7] high resolution spectroscopy,^[8] and in observational astronomy.^[9,10] On the fundamental side, the coherent assembly of UQOs devices can enable unique experimental arrangements to be devised for quantum measurements, for example to study nonclassical state emission from quantum cascade lasers. In this sense UQOs will greatly extend optoelectronic applications and quantum optics into the mid-infrared/Terahertz (THz) region.

In this work, we present the realization of an UQO system for data transmission in the 8–14 μm atmospheric window comprising a continuous wave (cw) quantum cascade (QC) laser, an external modulator, and a QC detector (Figure 1). In contrast to previous studies based on directly modulating a QC laser current,^[3,11–13] data-bits are written onto the laser emission in our system using a high frequency external modulator that operates by shifting the absorption of an optical transition in and out of the laser frequency. This device is designed to avoid charge displacement or electron depletion,^[14] and therefore it is characterized by an intrinsically large bandwidth and very low electrical power consumption in comparison with direct current modulation of the laser.^[11,15,16] This modulation scheme is a step forward to increase the bitrate for free-space communication with enhanced privacy in the mid-infrared.^[17] Using the set-up


H. Dely, T. Bonazzi, E. Rodriguez, D. Gacemi, Y. Todorov, A. Vasanelli, C. Sirtori

Laboratoire de Physique de l'Ecole Normale Supérieure
ENS, Université PSL, CNRS, Sorbonne Université, Université de Paris
24 rue Lhomond, Paris 75005, France
E-mail: carlo.sirtori@ens.fr

O. Spitz, F. Grillot
LTCI, Télécom Paris
Institut Polytechnique de Paris
19 Place Marguerite Perey, Palaiseau 91120, France

K. Pantzas, G. Beaudoin, I. Sagnes
Centre de Nanosciences et de Nanotechnologies
Université Paris Saclay – CNRS – Université Paris-Sud
10 Boulevard Thomas Gobert, Palaiseau 91120, France

L. Li, A. G. Davies, E. H. Linfield
School of Electronics and Electrical Engineering
University of Leeds
Woodhouse Lane, Leeds LS2 9JT, UK

 The ORCID identification number(s) for the author(s) of this article can be found under <https://doi.org/10.1002/lpor.202100414>

© 2021 The Authors. Laser & Photonics Reviews published by Wiley-VCH GmbH. This is an open access article under the terms of the Creative Commons Attribution License, which permits use, distribution and reproduction in any medium, provided the original work is properly cited.

DOI: 10.1002/lpor.202100414

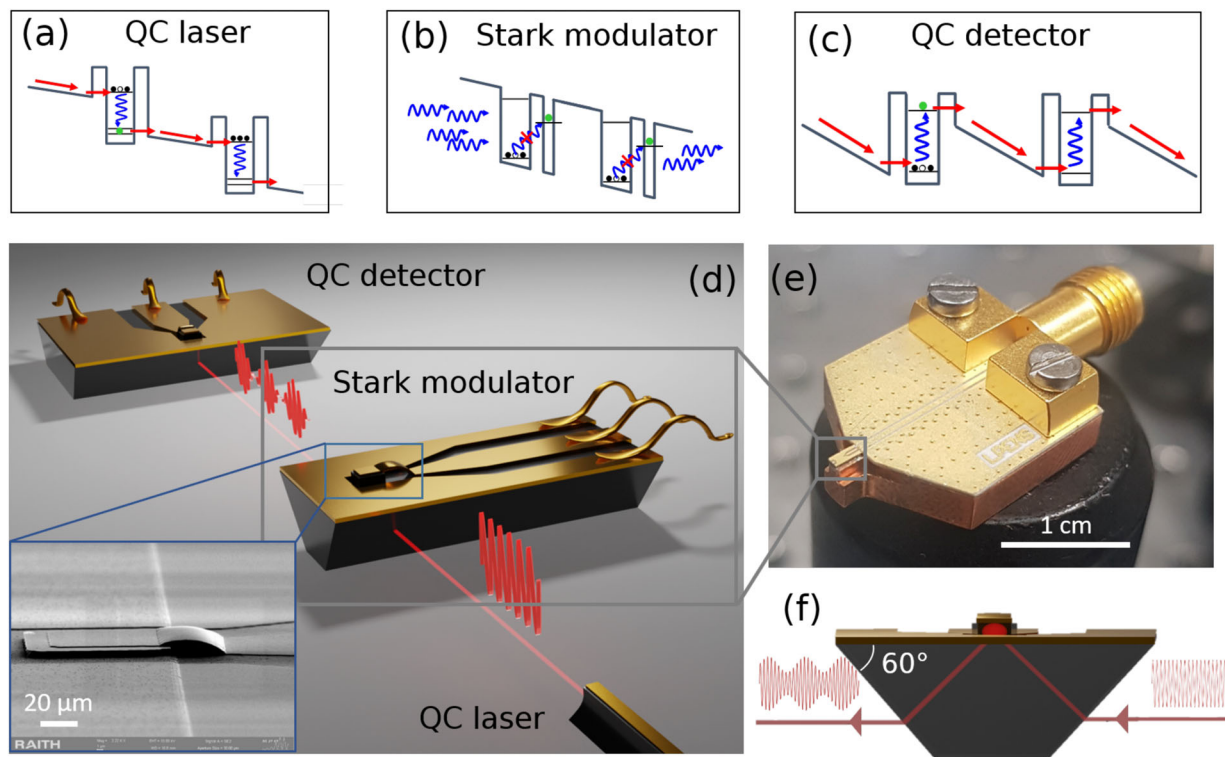


Figure 1. a–c) Sketch of the conduction band profile and relevant electronic states of a) a quantum cascade laser, b) Stark modulator, and c) quantum cascade detector. Right arrows indicate the electronic path in the structure, while the blue arrows indicate $9\ \mu\text{m}$ photons. d) Sketch of our experiment comprising QC laser, Stark modulator, and QC detector, all of them operating at room temperature and at the same wavelength, $9\ \mu\text{m}$ (138 meV). The laser is a commercial cw distributed feedback QC laser (Thorlabs QD9000HHL-B). The modulator and the detector have been specially designed, fabricated, and mounted to operate at high frequency. The inset shows a SEM image of the modulator connected via an air-bridge to the coplanar waveguide. e) RF packaging of the Stark modulator. f) Sketch of the light coupling geometry of the Stark modulator. This geometry complies with polarization selection rules.

illustrated in Figure 1, we have demonstrated a data rate transmission of $10\ \text{Gbit s}^{-1}$ on a single channel, with bit error rate of the order of 10^{-3} , compatible with common protocols for data transmission. To our knowledge, this is the fastest data transmission ever reported in this wavelength range paving the way for commercial communication systems outside the saturated near-infrared telecom bands. In the future, the photonic integration of these devices will further increase their performance and make it possible to extend the realm of quantum technologies deeper in the infrared and THz frequency ranges.^[18]

2. System Description and High Frequency Devices

Our system is sketched in Figure 1d. Light from a commercial distributed – feedback (DFB) QC laser (Figure 1a) impinges on the modulator (Figure 1b) that writes the information, which is subsequently read by the detector (Figure 1c). The laser is stabilized at $20\ ^\circ\text{C}$ and emits 84 mW. The beam propagation across the modulator is shown in Figure 1f: the light coupling into the modulator is through a 60° wedge to increase the coupling length and to facilitate the laser beam alignment. The insertion loss induced by the modulator in this geometry is $-4\ \text{dB}$. In order to operate at high frequency, the detector, and the modulator have been processed into mesa structures that are electrically connected to a $50\ \Omega$ coplanar waveguide through an air-bridge for a low - in-

ductance top contact.^[15,19] This is shown in the scanning electron microscope (SEM) image in the inset to Figure 1d. The device is then fixed on a custom-made holder and wire bonded onto an adapted printed circuit board (PCB) coplanar waveguide, as illustrated in Figure 1e. All devices are realized in III-V semiconductor heterostructures.

The detector is a GaAs/AlGaAs quantum cascade detector, based on a diagonal transition.^[20] The geometry for light coupling into the detector is a 45° polished facet, to comply with the polarization selection rules of optical transitions.^[21] When photons are absorbed they excite electrons from state 1 to state 2, as sketched in the band diagram of Figure 1c. After photoexcitation, electrons relax very rapidly by cascading toward the ground state of the following heterostructure period. This unipolar detector operates in the photovoltaic regime and yet has a very wideband frequency response.^[22] This is due to fast energy relaxation of the electrons and the asymmetry of the cascade region that acts as a pseudoelectric field driving the electrons in one direction only, giving rise to a photocurrent. The electron relaxation time from one period to the adjacent one is estimated to be shorter than 10 ps and therefore the intrinsic bandwidth is of the order of 100 GHz.^[15,19,23] However, the parasitic capacitance induced by the mesa structure limits the frequency range.

The frequency response, shown in Figure 2a, is almost flat up to the device cut-off, at 5 GHz for a $50 \times 50\ \mu\text{m}^2$ QC detector.

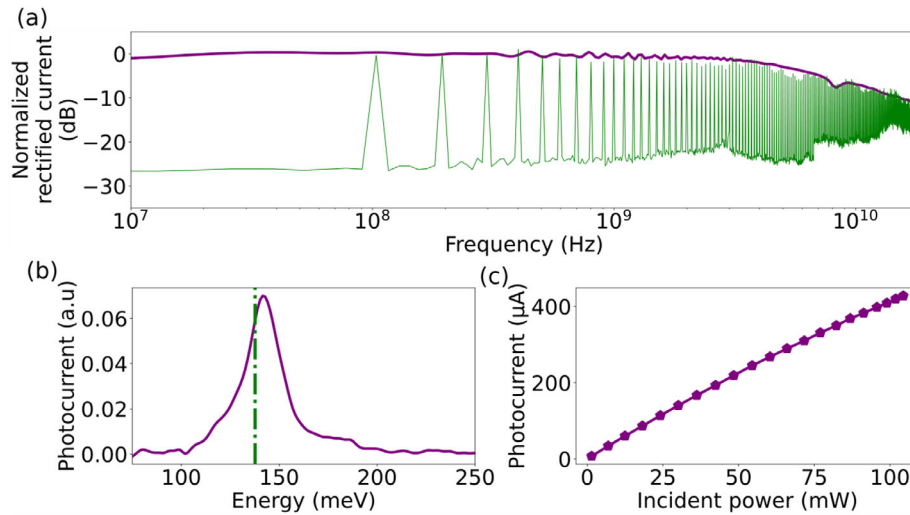


Figure 2. Quantum cascade detector characterisation at room temperature. a) Frequency response of the QC detector, measured by using rectification technique (violet line) and by using a mid-infrared frequency comb (green line) with teeth separated of 100 MHz. b) Measured photocurrent spectrum at room temperature, centred at an energy very close to the laser emission line (green dashed line). c) Photocurrent as a function of the incident laser power in cw operation.

Two different methods have been used to measure this response: a rectification technique (violet line) that relies on the nonlinear current–voltage (I – V) characteristic,^[19] and a direct optical measurement (green line) obtained by shining a mid-infrared frequency comb (Menlo System FC1500-ULN) onto the detector. The beating between the optical teeth appears as beatnotes separated by 100 MHz. Figure 2b shows the detector photocurrent spectrum centred at an energy very close to that of the laser emission (green dashed line), while panel (c) presents the photocurrent as a function of the incident cw laser power. The photocurrent is linear with the injected optical power up to 50 mW with a responsivity of 4.5 mA W⁻¹. Above 50 mW a mild decrease of the responsivity can be observed, associated with a thermal heating of the detector. This saturation is not a problem in our experiment as the highest optical power on the detector is less than 40 mW.

In order to exploit fully the large frequency bandwidth of our detector for data transmission, we have realized an extremely fast external modulator, based on a linear Stark effect,^[24,25] which avoids the implementation of gates for charge depletion, and hence reduces intrinsic parasitic capacitances. The modulator is an asymmetric quantum well^[26] made in the GaInAs/AlInAs materials system, n -doped at 1.5×10^{18} cm⁻³ in the wider well (inset to Figure 3a and the Experimental Section). This Stark shift originates from the fact that the probability density of electrons in state 1 is essentially localized in the large quantum well, while that in state 2 is in the thin well. Under an applied bias V , the energy shift of the transition E_{12} equals the drop in potential between the barycenters of the two distributions L_{bar} (which is approximately equal to the distance between the centres of the quantum wells) (see inset to Figure 3a)

$$E_{12}(V) = E_{12}(0) + e\Delta V_{\text{qw}} \quad (1)$$

with $\Delta V_{\text{qw}} = V \frac{L_{\text{bar}}}{L_{\text{struct}}}$ and L_{struct} the total thickness of the structure.

A shift of 30 meV can be seen in Figure 3a between the low energy absorption peaks of the two spectra measured at +4 V (blue line) and -4 V (black line). Therefore, the absorption at the optical transition E_{12} can be tuned in or out of resonance with the laser emission energy as a function of the applied bias as sketched in Figure 3b, illustrating the operation of the device as a function of time. This Stark shift of the E_{12} transition induces a modulation of the laser power absorbed by the device without any charge displacement from the doped well. In fact, the average electronic density is only displaced by a few Angstrom by the change in the applied bias, and lies entirely within the thickness of the quantum well (Figure 3b bottom panel). The speed of the modulator is therefore mostly limited by the geometric capacitance of the device, which has been confirmed by performing rectification measurements on devices with different mesa surfaces. The cut-off frequency is shown in Figure 3c (symbols) as a function of the inverse of the device surface, together with a simulation (black dashed line) that takes into account an extra capacitance of 61 fF, due to the wire bonding between the coplanar waveguides of the devices and the PCB board, in addition to the geometric capacitance (orange continuous line). The -3dB cut-off frequency is 4 GHz for an $80 \times 80 \mu\text{m}^2$ device, and almost 20 GHz for a $25 \times 25 \mu\text{m}^2$ device. For experimental convenience and given the bandwidth of the detector, all the following experiments were carried out using the $80 \times 80 \mu\text{m}^2$ modulator.

The modulation depth has been fully characterized by measuring the absorption under different applied bias, as shown in Figure 3d. For a positive bias of +6 V, the transition E_{12} is resonant with the laser photon energy (green dashed line) maximizing the absorption. For negative bias larger than -7 V, the absorption peak is strongly detuned from the laser emission and we obtain the largest transmission. The inset of Figure 3d presents the experimental (red symbols) and the calculated (red line) energy of the transition E_{12} as a function of the applied bias. From this plot we can extract a linear Stark shift of 3.9 meV V⁻¹.

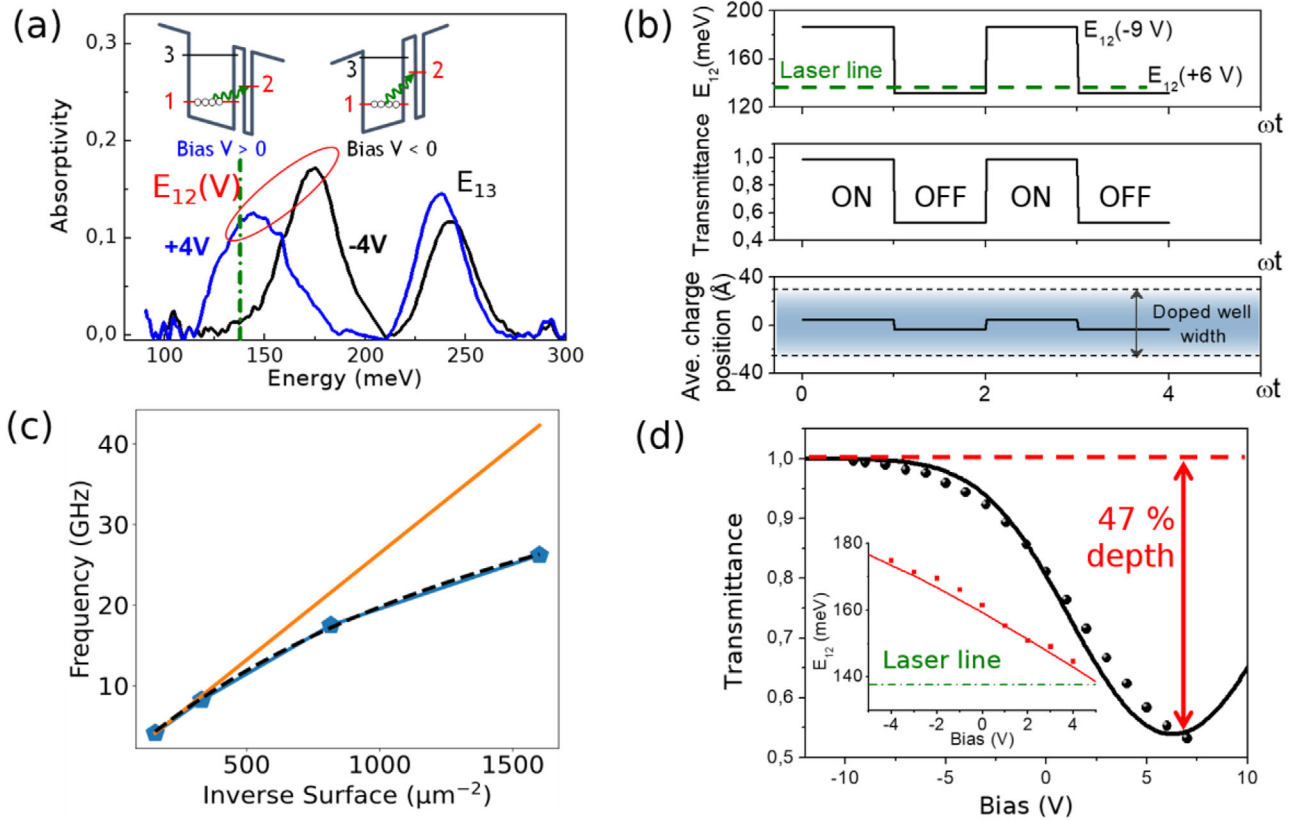


Figure 3. a) Absorption spectra measured at +4 V (blue line) and –4 V (black line). The green dashed line indicates the laser emission energy. The inset presents a sketch of the conduction band diagram for positive and negative voltage. The bias dependent optical transition involves states 1 and 2. b) Time operation of the Stark modulator. Top panel: the transition energy E_{12} is modulated by a time dependent applied bias and driven in and out of resonance with respect to the laser emission. Middle panel: time dependent modulated transmittance. Bottom panel: Average displacement of the electronic density. The shaded area indicates the width of the doped quantum well. c) Cut-off frequency as a function of the device size (symbols), simulated by only including the geometric capacitance of the device (orange continuous line), and simulated considering an extra capacitance of 61 fF due to nonideal capacitance effects for small-devices (black dashed line). d) Measured (dots) and simulated (line) transmittance through the modulator as a function of the applied voltage. The inset presents the transition energy E_{12} as a function of the applied voltage, as extracted from voltage dependent absorption measurements (red dots) and through simulation (line).

The absorption spectrum associated with the $1 \rightarrow 2$ transition can be written as a Gaussian function with voltage dependent peak energy, $E_{12}(V)$, and constant linewidth $\gamma = 17$ meV: $\alpha(V) = \alpha_0 \exp\left(-\frac{(E_{12}(V) - E_{\text{laser}})^2}{2\gamma^2}\right)$.^[24] The transmittance of the structure is $T(V) = \exp(-\alpha(V)L)$ and can be evaluated, by knowing the doping ($1.5 \times 10^{18} \text{ cm}^{-3}$) and the light-matter interaction length $L = 2L_{\text{qw}} N_{\text{qw}} \frac{\sin^2(\theta)}{\cos(\theta)}$, with θ the light propagation angle in the device (as sketched in Figure 1f), L_{qw} the thickness of the doped quantum well and N_{qw} the number of periods. The resulting voltage dependent transmittance is plotted in Figure 3d (black line).

The modulation depth has also been estimated by applying a square signal on the modulator and then measuring the optical power on the QC detector. Using the photocurrent measured when a –9 V bias is applied on the modulator as a reference, we retrieved the transmittance as plotted in Figure 3d (black dots), in very good agreement with our numerical estimations. From these data, the modulation depth, $\Delta P = \frac{P_{\text{max}} - P_{\text{min}}}{P_{\text{max}}}$, with P_{max} (P_{min}) the highest (lowest) transmitted optical power, is measured to be 47%. Our numerical estimations accurately reproduce these data.

Notably, the modulator shows an excellent linearity in transferring a microwave input to an amplitude signal on the optical carrier, an essential feature for the transmission of analog signals. This has been characterized by analysing the distortion of the optical signal as a function of the amplitude of a sinusoidal input on the modulator $V = V_m \cos(\omega t)$ (see the Supporting Information). When the modulator is biased close to the inflexion point of the transmittance as a function of voltage $T(V)$ in Figure 3d, the distortion appears as third order sidebands, which allows us to quantify the nonlinearity of the modulator. The sideband-to-carrier intensity ratio is over 20 dB at 9 V and therefore we can conclude that the modulator operates in its linear regime and does not lead to a significant distortion for a wide range of injected RF power. Furthermore, the QC detector does not introduce distortion as it is operated in its linear regime.

The optical frequency response of the full system for free-space data transmission, which has a cutoff at 2 GHz, is shown in Figure 4. The modulator, driven with a power sine wave, writes a signal onto the infrared beam emitted by the QC laser, which is then collected on the detector, and finally is analyzed

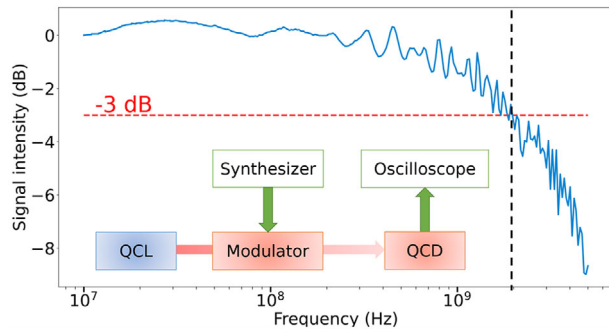


Figure 4. Optical frequency response of the full system for free space data transmission. Inset: Sketch of the system. The distance between the QC laser and the modulator is 70 cm and that between the modulator and the QC detector is 60 cm.

using a 16 GHz-cutoff oscilloscope (Teledyne Lecroy SDA Zi-B 16 GHz). In the following, we illustrate how using these UQO devices we were able to transmit 10 Gbit s^{-1} with a bit error rate (BER) below 4×10^{-3} in free space configuration.

3. Data Transmission

For the data transmission experiments, the modulator was connected to a pulse pattern generator that outputs 127 bit-long pseudorandom bit sequences (PRBS $2^7 - 1$) using a simple on-off keying (OOK) scheme. The latter consists only of “zeros” and “ones,” so that we have one bit per symbol. The bitrate ranges from 1 to 12 Gbit s^{-1} , limited by the pulse pattern generator. The modulated input signal from a random bit sequence at 7 Gbit s^{-1} and the output of the QC detector on the oscilloscope are shown in **Figure 5a**. The transmission characteristics are analyzed using eye diagrams and BER. **Figure 5c–f** displays eye diagrams taken at 7 and 11 Gbit s^{-1} . **Figure 5c,d** is the PRBS references on the oscilloscope, while **Figure 5e,f** is the corresponding optical eye diagrams of the modulated signal received on the QC detector. Eyes at 7 Gbit s^{-1} are well-opened, i.e., the ones and zeros are well-resolved, which is typical of a high-quality transmission, while at 11 Gbit s^{-1} a degradation can be seen from the BER (**Figure 5b**).

The BER presented on **Figure 5b** is obtained by acquiring $100 \mu\text{s}$ temporal traces for different bitrates and analyzing them with an algorithm that we developed ourselves (see the Experimental

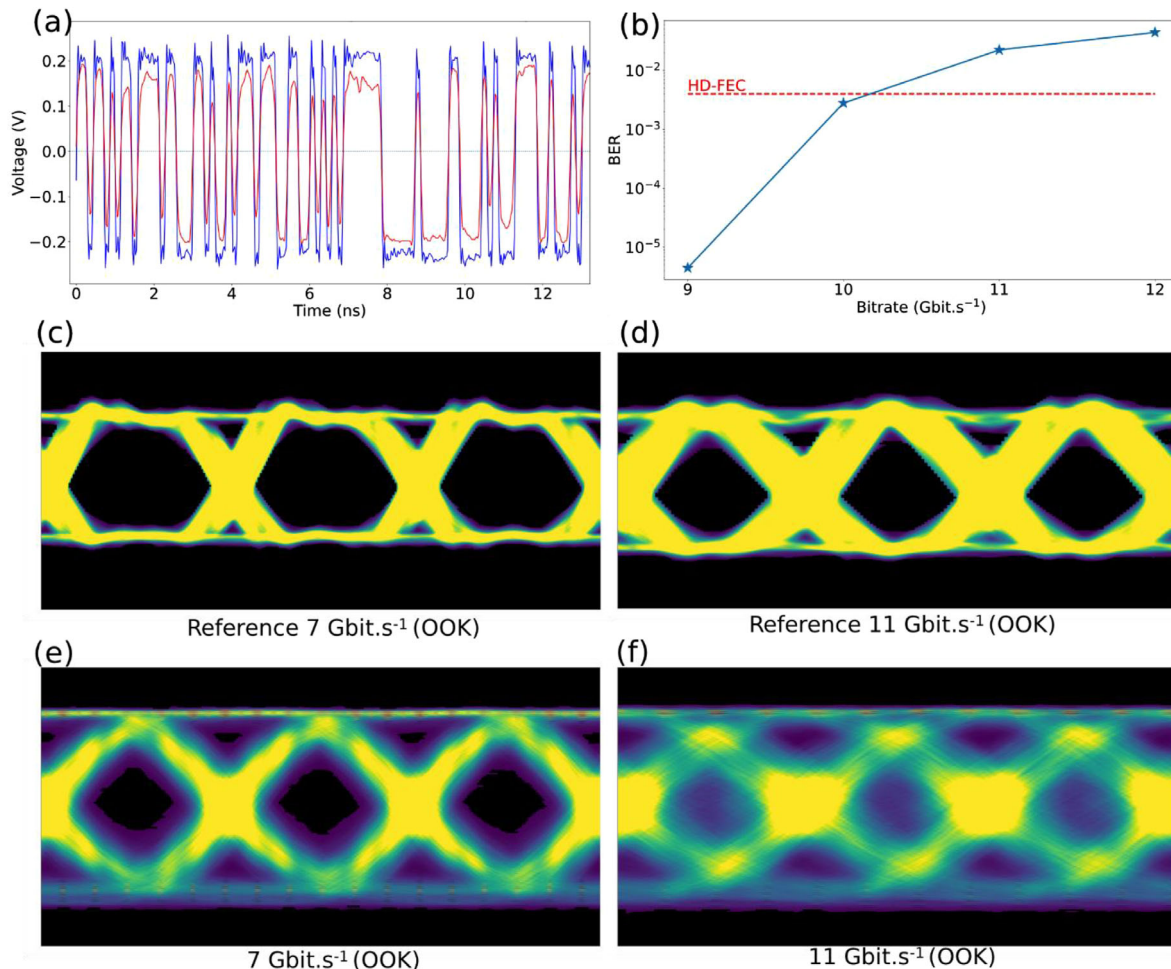


Figure 5. a) Modulated input signal (blue line) from a random bit sequence at 7 Gbit s^{-1} and output of the QC detector on the oscilloscope (red line). b) Bit error rate plotted as a function of the bitrate as extracted from a proprietary algorithm (blue line-symbols). The horizontal red line indicates the minimum affordable error rate by using hard-decision forward error correction (HD-FEC). c) Eye diagram of the reference signal at 7 Gbit s^{-1} and d) at 11 Gbit s^{-1} . e) Eye diagram measured at 7 Gbit s^{-1} and f) at 11 Gbit s^{-1} without any equalization.

Section). Below 9 Gbit s^{-1} the signal is error-free. Given that a $\text{BER} \leq 4 \times 10^{-3}$ can be corrected using error correction codes without excessive overhead,^[3,27] we achieved an error-free transmission up to 10 Gbit s^{-1} which is far beyond the state-of-the-art at this wavelength in free-space using either external^[28] or direct^[3] modulation, without any postprocessing nor equalization.

4. Conclusion

In conclusion, we have realized a data transmission system with an external amplitude modulator that operates in the mid-infrared ($\lambda = 9 \mu\text{m}$) and outperforms previous results obtained through external or direct modulation of laser current. This has been enabled by ultrafast UQO devices conceived with a multi-scale approach from nanometric quantum design to dedicated RF packaging. We have achieved a data-bit rate of 10 Gbit s^{-1} using an ON/OFF protocol that can be substantially improved further in the present devices, by multichannel modulation formats, for example through use of discrete multitone (DMT) modulation, and digital processing techniques,^[29,30] routinely implemented with specific integrated circuits. Moreover, the foreseeable bandwidth of these devices is in the 50–100 GHz range and therefore Terabit s^{-1} data rates should be within reach of this technology, thus positioning the UQO as a possible solution for 6G communications in unregulated frequency bands. Although our results have focused on data transmission, there is a broader scope of applications that arise from more complex UQO systems, involving different devices and different functions, such as heterodyne/homodyne detection for instance.

5. Experimental Section

Sample Description: The modulator device is made of $N_{\text{qw}} = 30$ periods of InGaAs wells and AlInAs barriers lattice-matched to InP. The thicknesses of the wells and barriers are **6.8/1.6/2.4/20** in nm (AlInAs barriers are in bold). The first underlined InGaAs layer is Si-doped to $1.5 \times 10^{18} \text{ cm}^{-3}$. The quantum wells and barriers are grown by metal-organic chemical vapour epitaxy on a Fe:InP substrate. Growth was performed in a Veeco D180 reactor.

The QCD consists in 12 periods of GaAs wells and AlGaAs barriers. The layer thicknesses in nm are **4.4/1.4/1.4/5.5/1.7/5.8/2.3/5.2/3.0/4.8** with the first underlined layer GaAs doped at $1 \times 10^{18} \text{ cm}^{-3}$. The AlGaAs barriers have a 35% Al concentration and are indicated in bold. The structure is grown by molecular beam epitaxy on a GaAs substrate.

Fabrication of the High Frequency Components: The modulator and the detector were processed into high-frequency coupled mesas in a similar fashion. For the modulator, square mesa regions of $80/55/35/25 \mu\text{m}$ of side were defined through optical lithography and chemically etched down to the bottom contact layer using $\text{H}_3\text{PO}_4:\text{H}_2\text{O}_2:\text{H}_2\text{O}$ (1:1:38). Then the half plane starting just below the mesa was protected with resist, allowing the contact to be etched away (using the same H_3PO_4 solution) as well as the epitaxial InP buffer (using pure HCl), down to the InP:Fe insulating wafer. The situation following this step is visible in the SEM picture in the inset to Figure 1d. After depositing a sacrificial support of reflowed S1818 resist for the air bridge, the Ti/Au 50 Ω coplanar waveguide was evaporated in one step using negative resist AZ5214 E for patterning. A photoresist stripper (SVC 14) was preferred to the standard acetone lift off to ensure that the bridge was properly freed from resist.

The detector underwent the same processing except for the etching step, where the mesa was physically etched (Cl-based ICP). Furthermore, there was no need for buffer etching since the AlGaAs layer below the contact was already insulating.

Spectra Under Bias: Measurements were taken using a Fourier transform infrared spectrometer (FTIR). The sample was processed into 1 mm large ridges to accommodate for the large beam spot, then lapped in a multipass configuration and connected to the electrodes via wire bonding. The sample was cooled to 78 K to limit leakage current under large bias.

Simulation of the Modulator Absorption Under Bias: The transmittance of the modulator was simulated from Beer–Lambert’s law for a Gaussian intersubband absorption spectrum which linearly shifts under bias (3.9 meV V^{-1} for this Stark shift): $T = \exp(-\alpha_0 \times \exp(-\frac{(E_{\text{laser}} - E_{12})^2}{2\Gamma^2})) \times L$.

The absorption coefficient was calculated as $\alpha_0 = \frac{n_{3D} e^2 \hbar}{2\epsilon_0 c \Gamma m^*} \frac{f_{12}}{\sqrt{2\pi} \Gamma}$ with $n_{3D} = 1.5 \times 10^{18} \text{ cm}^{-3}$ the electron concentration, $\eta = 3.1$ the refractive index, $\Gamma = 17 \text{ meV}$ the linewidth of the transition (considered constant), and $f_{12} = 0.64$ the oscillator strength of the transition 1–2 calculated at 0 V. Finally, the interaction length was taken as $L = 2L_{\text{qw}} N_{\text{qw}} * \frac{\sin^2(\theta)}{\cos \theta}$ with $\theta = 69.3^\circ$.

Rectification Bandwidth Measurements: A sine radiofrequency signal generated with a synthesizer (Anritsu MG3693B) was injected into the device through a wideband bias-tee (SHF-BT45). The nonlinear I – V characteristic of the devices generates a rectified DC current $I_{\text{DC}} \propto |H(\omega)|^2$ proportional to the squared voltage transfer function $H(\omega)$ of the device. This current was collected from the bias-tee DC connector on a sourcemeter (Keithley 2450).

Full Setup Optical Bandwidth Measurements: The sine wave synthesizer and a sourcemeter were connected to the modulator through a bias-tee. The same arrangement was performed for the detector with a high-speed oscilloscope (Teledyne LeCroy SDA16 Zi-B) in place of the synthesizer. A temporal trace of the AC signal generated by the detector was acquired for $100 \mu\text{s}$ at 40 GS s^{-1} on the oscilloscope and sent to the computer. Finally, a Fourier transform was performed to extract the relevant frequency component.

Data Transfer Measurements: The same arrangement as the one employed for the optical bandwidth was used, replacing the synthesizer with a pseudorandom bit sequence (PRBS) pulse pattern generator (Anritsu MP1763B), which delivers a peak-to-peak voltage of 0.2 V on 50 Ω , which is then amplified with a +25dB amplifier. The peak-to-peak voltage on the modulator (which has an impedance of 3.5 k Ω) is then 15 V. A DC offset of 1.1 V was added to compensate for distortion and saturation. A 127-bit sequence which is well suited for the system, which presents a lower cutoff at 100 MHz, was used.

The laser power incident on the modulator was about 84 mW, kept constant for all data bitrates. The received optical power (after the modulator) was about 33 mW.

The quality of the transmission was first analyzed using the oscilloscope data analysis software to obtain the bit error rate, and then a 100 μs temporal trace was acquired and analyzed using a home-made algorithm to compute another estimation of the bit error rate.

Bit Error Rate Algorithm: Measurements were performed with a home-made Matlab program. Given the timetraces from the oscilloscope, this program resamples the data at a constant sample-per-bit ratio and performs a time-correlation calculation on the input and received signals to calculate the delay between them and realign them accordingly. The sequences of bits associated with each signal were determined and finally compared to each other to get the bit error rate after selecting the most appropriate amplitude threshold.

Supporting Information

Supporting Information is available from the Wiley Online Library or from the author.

Acknowledgements

H.D. and T.B. contributed equally to this work. H.D., D.G., A.V., and C.S. warmly acknowledge fruitful discussions with Richard Schatz and the

cFlow consortium. O.S. and F.G. wish to thank Dr. Elie Awwad and Andreas Herdt for fruitful discussions. The authors acknowledge financial support from the ENS-Thales Chair, ANR project LIGNEDEMIR (ANR-18-CE09-0035), FET-Open 2018–2020 Horizon 2020 project cFLOW, CNRS Renatech network, Ile-de-France Region in the framework of DIM SIRTEQ, and the EPSRC programme grant “HyperTerahertz” (No. EP/P021859/1).

Conflict of Interest

The authors declare no conflict of interest.

Data Availability Statement

The data that support the findings of this study are available from the corresponding author upon reasonable request.

Keywords

free space data transmission, mid-infrared, quantum devices

Received: July 29, 2021

Revised: December 1, 2021

Published online:

- [1] D. Palaferri, Y. Todorov, A. Bigioli, A. Mottaghizadeh, D. Gacemi, A. Calabrese, A. Vasanelli, L. Li, A. G. Davies, E. H. Linfield, F. Kapsalidis, M. Beck, J. Faist, C. Sirtori, *Nature* **2018**, 556, 85.
- [2] A. Bigioli, G. Armaroli, A. Vasanelli, D. Gacemi, Y. Todorov, D. Palaferri, L. Li, A. G. Davies, E. H. Linfield, C. Sirtori, *Appl. Phys. Lett.* **2020**, 116, 161101.
- [3] X. Pang, O. Ozolins, L. Zhang, R. Schatz, A. Udalcovs, X. Yu, G. Jacobsen, S. Popov, J. Chen, S. Lourdudoss, *Phys. Status Solidi A* **2021**, 218, 2000407.
- [4] R. Martini, C. Bethea, F. Capasso, C. Gmachl, R. Paiella, E. A. Whittaker, H. Y. Hwang, D. L. Sivco, J. N. Baillargeon, A. Y. Cho, *Electron. Lett.* **2002**, 38, 181.
- [5] R. Martini, E. A. Whittaker, *J. Opt. Fiber Commun. Rep.* **2005**, 2, 279.
- [6] A. Delga, L. Leviandier, *Proc. SPIE* **2019**, 10926, 1092617.
- [7] A. Diaz, B. Thomas, P. Castillo, B. Gross, F. Moshary, *Appl. Phys. B* **2016**, 122, 121.
- [8] G. Villares, A. Hugi, S. Blaser, J. Faist, *Nat. Commun.* **2014**, 5, 5192.
- [9] P. Krötz, D. Stupar, J. Krieg, G. Sonnabend, M. Sornig, F. Giorgetta, E. Baumann, M. Giovannini, N. Hoyler, D. Hofstetter, R. Schieder, *Appl. Phys. B* **2008**, 90, 187.
- [10] D. D. S. Hale, M. Bester, W. C. Danchi, W. Fitelson, S. Hoss, E. A. Lipman, J. D. Monnier, P. G. Tuthill, C. H. Townes, *Astrophys. J.* **2000**, 537, 998.
- [11] R. Paiella, R. Martini, F. Capasso, C. Gmachl, H. Y. Hwang, D. L. Sivco, J. N. Baillargeon, A. Y. Cho, E. A. Whittaker, H. C. Liu, *Appl. Phys. Lett.* **2001**, 79, 2526.
- [12] F. Capasso, R. Paiella, R. Martini, R. Colombelli, C. Gmachl, T. L. Myers, M. S. Taubman, R. M. Williams, C. G. Bethea, K. Unterrainer, H. Y. Hwang, D. L. Sivco, A. Y. Cho, A. M. Sergent, H. C. Liu, E. A. Whittaker, *IEEE J. Quantum Electron.* **2002**, 38, 511.
- [13] R. Martini, C. Gmachl, J. Falciglia, F. G. Curti, C. G. Bethea, F. Capasso, E. A. Whittaker, R. Paiella, A. Tredicucci, A. L. Hutchinson, D. L. Sivco, A. Y. Cho, *Electron. Lett.* **2001**, 37, 191.
- [14] S. Pirotta, N.-L. Tran, A. Jollivet, G. Biasiol, P. Crozat, J.-M. Manceau, A. Bousseksou, R. Colombelli, *Nat. Commun.* **2021**, 12, 799.
- [15] E. Rodriguez, A. Mottaghizadeh, D. Gacemi, D. Palaferri, Z. Asghari, M. Jeannin, A. Vasanelli, A. Bigioli, Y. Todorov, M. Beck, J. Faist, Q. J. Wang, C. Sirtori, *ACS Photonics* **2018**, 5, 3689.
- [16] B. Hinkov, A. Hugi, M. Beck, J. Faist, *Opt. Express* **2016**, 24, 3294.
- [17] O. Spitz, A. Herdt, J. Wu, G. Maisons, M. Carras, C.-W. Wong, W. Elsässer, F. Grillot, *Nat. Commun.* **2021**, 12, 3327.
- [18] A. Spott, E. J. Stanton, N. Volet, J. D. Peters, J. R. Meyer, J. E. Bowers, *IEEE J. Select. Topics Quantum Electron.* **2017**, 23, 1.
- [19] H. C. Liu, J. Li, M. Buchanan, Z. R. Wasilewski, *IEEE J. Quantum Electron.* **1996**, 32, 1024.
- [20] P. Reininger, B. Schwarz, H. Detz, D. MacFarland, T. Zederbauer, A. M. Andrews, W. Schrenk, O. Baumgartner, H. Kosina, G. Strasser, *Appl. Phys. Lett.* **2014**, 105, 091108.
- [21] M. Helm, *Intersubband Transitions in Quantum Wells: Physics and Device Applications*, Vol. 62, Academic Press, San Diego, CA **2000**.
- [22] T. Dougakiuchi, A. Ito, M. Hitaka, K. Fujita, M. Yamanishi, *Appl. Phys. Lett.* **2021**, 118, 041101.
- [23] M. Hakl, Q. Lin, S. Lepillet, M. Billet, J.-F. Lampin, S. Pirotta, R. Colombelli, W. Wan, J. C. Cao, H. Li, E. Peytavit, S. Barbieri, *ACS Photonics* **2021**, 8, 464.
- [24] J. Teissier, S. Laurent, C. Manquest, C. Sirtori, A. Bousseksou, J. R. Coudeville, R. Colombelli, G. Beaudoin, I. Sagnes, *Opt. Express* **2012**, 20, 1172.
- [25] J. Teissier, S. Laurent, C. Sirtori, H. Debrégeas-Sillard, F. Lelarge, F. Brillouet, R. Colombelli, *Appl. Phys. Lett.* **2009**, 94, 211105.
- [26] C. Sirtori, F. Capasso, D. L. Sivco, A. L. Hutchinson, A. Y. Cho, *Appl. Phys. Lett.* **1992**, 60, 151.
- [27] O. Ozolins, L. Zhang, A. Udalcovs, H. Louchet, T. Dippon, M. Gruen, X. Pang, R. Schatz, U. Westergren, S. Xiao, S. Popov, J. Chen, *Eur. Conf. Opt. Commun.* **2019**, 257, 257.
- [28] T. Li, M. Nedeljkovic, N. Hattasan, W. Cao, Z. Qu, C. G. Littlejohns, J. S. Penades, L. Mastronardi, V. Mittal, D. Benedikovic, D. J. Thomson, F. Y. Gardes, H. Wu, Z. Zhou, G. Z. Mashanovich, *Photonics Res.* **2019**, 7, 828.
- [29] X. Pang, O. Ozolins, R. Schatz, J. Storck, A. Udalcovs, J. R. Navarro, A. Kakkar, G. Maisons, M. Carras, G. Jacobsen, S. Popov, S. Lourdudoss, *Opt. Lett.* **2017**, 42, 3646.
- [30] F. Chang, K. Onohara, T. Mizuochi, *IEEE Commun. Mag.* **2010**, 48, 548.